Numerical study of boundary layer interaction with shocks – method improvement and test computation

By N. A. Adams

1. Motivation and objectives

The general motivation of this work has been outlined in Adams (1994). The objective is the development of a high-order and high-resolution method for the direct numerical simulation of shock turbulent-boundary-layer interaction. Details concerning the spatial discretization of the convective terms can be found in Adams and Shariff (1995). The computer code based on this method as introduced in Adams (1994) was formulated in Cartesian coordinates and thus has been limited to simple rectangular domains. For more general two-dimensional geometries, as a compression corner, an extension to generalized coordinates is necessary. To keep the requirements or limitations for grid generation low, the extended formulation should allow for non-orthogonal grids. Still, for simplicity and cost efficiency, periodicity can be assumed in one cross-flow direction.

For easy vectorization, the compact-ENO coupling algorithm as used in Adams (1994) treated whole planes normal to the derivative direction with the ENO scheme whenever at least one point of this plane satisfied the detection criterion. This is apparently too restrictive for more general geometries and more complex shock patterns. Here we introduce a localized compact-ENO coupling algorithm, which is efficient as long as the overall number of grid points treated by the ENO scheme is small compared to the total number of grid points.

Validation and test computations with the final code are performed to assess the efficiency and suitability of the computer code for the problems of interest. We define a set of parameters where a direct numerical simulation of a turbulent boundary layer along a compression corner with reasonably fine resolution is affordable.

2. Accomplishments

2.1 Generalized coordinates

The fundamental equations solved are the conservation equations for mass, momentum, and energy in generalized coordinates

$$\frac{\partial}{\partial t}\frac{U}{J}+\frac{\partial}{\partial x}\frac{F_E}{J}+\frac{\partial}{\partial y}\frac{G_E}{J}+\frac{\partial}{\partial z}\frac{H_E}{J}=\frac{\partial}{\partial x}\frac{F_S}{J}+\frac{\partial}{\partial y}\frac{G_S}{J}+\frac{\partial}{\partial z}\frac{H_S}{J} \qquad (1)$$

where the conservative variables are

$$U = \begin{bmatrix} \rho \\ \rho u \\ \rho v \\ \rho w \\ E \end{bmatrix} \quad , \tag{2}$$

with $E = \frac{1}{\kappa - 1} p + \frac{\rho}{2}(u^2 + v^2 + w^2)$. Considering only spanwise periodic configurations we limit the coordinate generalization to the (x, z)-plane. The convective fluxes are given by

$$F_E = \begin{bmatrix} \rho(u\xi_x + w\xi_z) \\ \rho u(u\xi_x + w\xi_z) + p\xi_x \\ \rho v(u\xi_x + w\xi_z) \\ \rho w(u\xi_x + w\xi_z) \\ (E + p)(u\xi_x + w\xi_z) \end{bmatrix} \quad , \tag{3}$$

and similarly for G_E and H_E. The viscous fluxes are given by

$$F_S = \begin{bmatrix} \tau_{xx}\xi_x + \tau_{xz}\xi_z \\ \tau_{xy} \\ \tau_{xz}\xi_x + \tau_{zz}\xi_z \\ -q_x\xi_x - q_z\xi_z + (u\tau_{xx} + v\tau_{xy} + w\tau_{xz})\xi_x + (u\tau_{xz} + v\tau_{yz} + w\tau_{zz})\xi_z \end{bmatrix} \quad , \tag{4}$$

and similarly G_S and H_S. The Jacobian of the coordinate transformation is

$$J = \xi_x\zeta_z - \xi_z\zeta_x \quad . \tag{5}$$

The stresses are defined as

$$\tau_{xx} = \frac{\mu}{Re}\left[\frac{4}{3}\left(\frac{\partial u}{\partial \xi}\xi_x + \frac{\partial u}{\partial \zeta}\zeta_x\right) - \frac{2}{3}\frac{\partial v}{\partial \eta}\eta_y - \frac{2}{3}\left(\frac{\partial w}{\partial \xi}\xi_z + \frac{\partial w}{\partial \zeta}\zeta_z\right)\right] \quad , \tag{6}$$

with analogous definitions for τ_{yy} and τ_{zz} ;

$$\tau_{xy} = \frac{\mu}{Re}\left[\left(\frac{\partial v}{\partial \xi}\xi_x + \frac{\partial v}{\partial \zeta}\zeta_x\right) + \frac{\partial u}{\partial \eta}\eta_y\right] \quad , \tag{7}$$

and similarly for τ_{xz}, τ_{yz}, and τ_{xz}. The heat fluxes are defined as

$$q_x = -\frac{\mu}{(\kappa - 1)M_\infty^2 PrRe}\left(\frac{\partial T}{\partial \xi}\xi_x + \frac{\partial T}{\partial \zeta}\zeta_x\right) \quad , \tag{8}$$

q_y and q_z analogously. The viscosity is calculated according to Sutherland's law. We also assume the thermal equation of state for perfect gases to be valid.

Given a wall-normal temperature gradient distribution $\partial T/\partial n$, a von Neumann condition for the temperature is imposed by setting

$$T_\zeta = \frac{\sqrt{\zeta_x^2 + \zeta_z^2}\frac{\partial T}{\partial n} - (\xi_x\zeta_x + \xi_z\zeta_z)\frac{\partial T}{\partial \xi}}{\zeta_x^2 + \zeta_z^2} \tag{9}$$

whenever it appears during the computation of heat flux and stress terms (due to the temperature dependence of the viscosity).

2.2 Grid generation

For the generation of an analytic mapping of the computational domain onto the physical domain we follow a simple algebraic procedure. We restrict our interest to channel-like geometries where lower and upper boundary can be approximated by simple functions. The mapping is non-conformal and thus the orthogonal partition of the computational domain will be mapped onto a non-orthogonal partition of the physical domain in general. The mapping consists of two steps: (1) the computational domain $\{\xi, \zeta\} \in [0,1] \times [0,1]$ with a uniformly spaced partitioning is mapped onto an intermediate space with non-uniform partitioning $\{s, t\} \in [0,1] \times [0,1]$; (2) the intermediate space $\{s, t\}$ is mapped onto the physical space $\{x, z\}$. Using a linear blending function between lower and upper boundary, we define this latter mapping function by

$$x(\xi, \zeta) = (1-t)x_l(s) + t x_u(s) \tag{10}$$

$$z(\xi, \zeta) = t z_l(s) + (1-t) z_u(s) \ , \tag{11}$$

the indices l and u indicate that the functions are to be taken at the lower and upper boundary, respectively. The components of the Jacobi matrix are then given by

$$\frac{\partial(x,z)}{\partial(\xi,\zeta)} = \begin{bmatrix} \frac{\partial x}{\partial \xi} & \frac{\partial x}{\partial \zeta} \\ \frac{\partial z}{\partial \xi} & \frac{\partial z}{\partial \zeta} \end{bmatrix} \ . \tag{12}$$

Later the metric coefficients will be needed, which are the components of the inverse Jacobi matrix,

$$\frac{\partial(\xi,\zeta)}{\partial(x,z)} = \mathrm{Adj}\left(\frac{\partial(x,z)}{\partial(\xi,\zeta)}\right)\left[\mathrm{Det}\left(\frac{\partial(x,z)}{\partial(\xi,\zeta)}\right)\right]^{-1} \tag{13}$$

and the Jacobian

$$J(\xi,\zeta) = \mathrm{Det}\left(\frac{\partial(\xi,\zeta)}{\partial(x,z)}\right) \ . \tag{14}$$

For the point distributions along the parameter lines $s(\xi)$ along the lower and upper boundary, we define

$$s(\xi) = a\xi + b + c_1 \sinh[g_3(\xi)] \tag{15}$$

and its derivative

$$\frac{ds(\xi)}{d\xi} = a + \frac{c_1}{c_3}\cosh[g_3(\xi)] \ . \tag{16}$$

The following abbreviations are used:

$$g_3(\xi) = \frac{\xi - c_2}{c_3} \tag{17}$$

$$a = 1 - c_1\left[\sinh\left(\frac{c_2}{c_3}\right) + \sinh\left(\frac{1-c_2}{c_3}\right)\right] \tag{18}$$

$$b = c_1 \sinh\left(\frac{c_2}{c_3}\right) \ . \tag{19}$$

If we consider compression corner geometries, then c_1 and c_3 are parameters that tune the grid point condensation around the corner point x_c. It coincides with the zero of $\sinh[g_3(\xi)]$, which is the condition from which c_2 is computed by solving

$$x_c - x(c_2) = 0 \tag{20}$$

for c_2. Knowing all parameters we define the variation of x along the lower or upper boundary in terms of the parameter s as

$$x(s) = Ls \ , \tag{21}$$

where L is the maximum value x assumes on the lower or upper boundary, respectively. Having obtained $x(s)$ we get $z(s)$ in the following manner.

$$z(x) = d_2 \left[x + \frac{1}{d_1}\ln\left(\cosh\left(d_1 x - x_c\right)\right) + d_3\right] \ . \tag{22}$$

A corner singularity in the mapping is avoided by prescribing a finite curvature r_c at $\{x_c, 0\}$. The ramp endpoint is given by $\{L, \sin(\phi)(L - x_c)\}$, where ϕ is the ramp angle in physical space $\{x, z\}$. The parameter d_2 is computed from the condition

$$z(L) = \sin(\phi)(L - x_c) \ . \tag{23}$$

Finally one sets

$$d_1 = \frac{(1 + d_2^2)^{\frac{3}{2}}}{r_c} \tag{24}$$

and

$$d_3 = -\frac{d_2}{d_1}\ln(\cosh(d_1 x_c)) \ . \tag{25}$$

In the transversal direction we introduce the parameter function $t(\zeta)$

$$t(\zeta) = \frac{z_{1/2}}{z_1} h_1(\zeta)\left[\left(1 - \frac{z_{1/2}}{z_1}\right) + h_1(\zeta)\left(\frac{2z_{1/2}}{h1} - 1\right)\right]^{-1} \tag{26}$$

and its derivative

$$\frac{dt(\zeta)}{d\zeta} = \frac{z_{1/2}}{z_1}\left(\frac{1 - z_{1/2}}{z_1}\right)\left(c + \frac{e_1}{e_3}\cosh(h_2(\zeta))\right) \times \tag{27}$$

$$\times \left[\left(1 - \frac{z_{1/2}}{z_1}\right) + \left(\frac{2z_{1/2}}{z_1} - 1\right) h_1(\zeta)\right]^{-2} \ . \tag{28}$$

Herein following abbreviations and parameters are used: e_1 and e_3 control the grid stretching at a point $\{0, z_{mv}\}$ similar to d_1 and d_3; about half of the grid points are between $\{0,0\}$ and $\{0, z_{1/2}\}$. $\{0, z_1\}$ is the upper-left corner point. The auxiliary functions h_1 and h_2 are defined as

$$h_1(\zeta) = c\zeta + d + e_1 \sinh(h_2(\zeta)) \tag{29}$$

and

$$h_2(\zeta) = \frac{\zeta - e_2}{e_3} \ . \tag{30}$$

The constants c and d are given by

$$c = 1 - e_1 \left[\sinh\left(\frac{1-e_2}{e_3}\right) + \sinh\left(\frac{e_2}{e_3}\right) \right] \tag{31}$$

and

$$d = e_1 \sinh\left(\frac{e_2}{e_3}\right) \ . \tag{32}$$

Given z_{mv}, the parameter e_2 is computed from the condition that the argument of $z(\zeta) = z_{mv}$ coincides with $h_2(\zeta) = 0$, i.e. e_2 is obtained by solving

$$z_{mv} - z_1 t(e_2) = 0 \ . \tag{33}$$

2.3 Local compact-ENO coupling

The principle of the coupling between ENO-scheme and the compact finite-difference scheme is discussed in Adams and Shariff (1995). The actual implementation with a reasonable capability for vector optimization is more involved. Let us consider the one dimensional and one component problem. Given the flux F on the grid $\{x_j\}$, its derivative for x is approximated by

$$\frac{\partial F}{\partial x} \doteq P_N[F] = \mathbf{M}_L^{-1} \mathbf{M}_R F \tag{34}$$

Assume that $\{x\}_E = \{x_p, \ldots, x_q\}_1 \cup \cdots \cup \{x_r, \ldots, x_s\}_{n_E}$ is the union of regions of points where the flux derivatives are approximated by the ENO scheme. If a shock detection algorithm has detected a point x_i to be treated by the ENO scheme, υ_i is set true and we define a topology vector Υ by

$$\Upsilon = \{\upsilon_i\} \ . \tag{35}$$

This vector has n_E unity blocks with dimensions $N_{n_E} \geq 2N_{sep}+1$, where N_{sep} is the dimension of the padding on both sides of ENO regions (Adams and Shariff, 1995). Whenever we have $\upsilon_i = 1$ for a certain grid point, we calculate $P_N[F]_i = P_N^{ENO}[F]_i$ from the ENO scheme.

The effect of the compact-ENO coupling on Eq. (34) is that the ith component of $\mathbf{M}_R F$ is replaced by the flux derivative at i calculated with the ENO scheme whenever υ_i is 1. The row i of $\mathbf{M}_L$ has then to become unity so that the ENO flux derivative $P_N^{ENO}[F]$ is exactly returned when Eq. (34) is solved for $P_N[F]$. We defining a correction matrix $\mathbf{BCD}$, which changes the rows i of $\mathbf{M}_L$ to unity whenever υ_i is true by its dyadic decomposition into the matrices $\mathbf{B}$, $\mathbf{D}$, and $\mathbf{C}$, the dimensions of which are given below. With this definition the fundamental equation for the computation of flux derivatives of the hybrid scheme can be written as

$$(\mathbf{M}_L - \mathbf{BDC})P_N[F] = \mathbf{M}_R F + \Upsilon(P_N^{ENO}[F] - \mathbf{M}_R F) \ . \tag{36}$$

The rank of the correction matrix $\mathbf{BCD}$ is $\sum_{\nu=1}^{n_E} N_\nu = m_E$. It is evident that Eq. (36) returns the ENO flux derivatives exactly at points i whenever $\upsilon_i = 1$.

To solve Eq. (36) efficiently we make use of the identity by Frobenius and Schur (Zurmühl and Falk, 1984, pg. 308,312) which allows to compute $(\mathbf{M}_L - \mathbf{BDC})^{-1}$ by using the inverse of $\mathbf{M}_L$ corrected by a the inverse of a rank m_E matrix $\mathbf{R}$. If $m_E << N$ this procedure is more efficient for multi-dimensional problems by using the precomputed inverse of $\mathbf{M}_L$ than inverting the LHS-matrix of Eq. (36).

The matrices $\mathbf{B}$, $\mathbf{D}$ and $\mathbf{C}$ are defined as follows:

$$\underbrace{\mathbf{B}}_{m_E \times N} = \sum_{\nu=1}^{m_E} \Upsilon \mathbf{e}_\nu^T \ , \tag{37}$$

$$\underbrace{\mathbf{D}}_{m_E \times m_E} = \underbrace{\mathbf{I}}_{m_E \times m_E} = \mathbf{I}_{m_E} \tag{38}$$

and

$$\underbrace{\mathbf{C}}_{m_E \times N} = \mathbf{B}^T(\mathbf{M}_L - \mathbf{I}) \ . \tag{39}$$

Here we define $\mathbf{e}_\nu$ as the m_E-component vector with its ν component equal to unity the rest being zero.

The solution algorithm for Eq. (36) according to (Zurmühl and Falk, 1984) is the following:
(0.) calculate the uncorrected solution vector $\mathbf{y}$ from

$$\mathbf{M}_L \mathbf{y} = \mathbf{M}_R F + \Upsilon(P_N^{ENO}[F] - \mathbf{M}_R F)$$

by direct inversion using the precomputed LU-decomposition of $\mathbf{M}_L$;
(1.) compute matrix $\mathbf{V}$ from

$$\mathbf{M}_L \mathbf{V} = \mathbf{B}$$

by direct inversion using the precomputed LU-decomposition of $\mathbf{M}_L$;
(2.) generate the rank m_E correction matrix $\mathbf{R}$ from

$$\mathbf{R} = \mathbf{I}_{m_E} - \mathbf{CV} \ ;$$

TABLE 1. Flow parameters for $M_\infty = 6$ ramp.

quantity	value	comment
T^*_∞	57.32K	free stream temperature
M_∞	6	free stream Mach number
p^*_∞	681.15Pa	free stream pressure
Pr	0.7	Prandtl number
κ	1.4	ratio of specific heats
R	287.03	gas constant
μ^*_∞	$3.77 \cdot 10^{-6}$kg/m/s	free stream viscosity
S^*	110.4K	Sutherland constant
Re_{ξ_0}	100000	running length Reynolds number
Re_{δ_1}	5255	reference Reynolds number
δ^*_1	$5.2554 \cdot 10^{-4}$m	reference length
ξ_0	19.03	inflow dist. from lead. edge
L_1	57.14	length of first ramp segment
L_2	120	length of second ramp segment
ϕ	7.5^o	ramp deflection angle

(3.) get the solution correction vector $\mathbf{z}$ from

$$\mathbf{Rz} = \mathbf{Cy}$$

(note that $\mathbf{R}$ is usually fully occupied so that this procedure is only efficient if $m_E << N$);
(4.) find the solution vector from

$$P_N[F] = \mathbf{y} + \mathbf{z} \ .$$

For a multidimensional problem all points in index planes normal to the derivative direction are gathered and a vector loop is spanned over these.

2.4 Code validation

Similar to Adams (1994) we validate the generalized coordinate code by comparison with a steady state solution. Experimental and numerical data for comparison are taken from the computational and experimental results of a laminar boundary layer along a 7.5^o compression corner at $M_\infty = 6$ by Simeonides *et al.* (1994). We emphasize that for the results presented in this section time-accurate and low-dissipation methods have been used. The computations have thus been halted before a true steady state has been reached (residual about 10^{-4}). The flow parameters are given in Table 1 (reference length is δ^*_1, dimensional quantities are marked with a star).

In Fig. 2 the grid generated by the algorithm in section 2.2 is shown (each 4th grid line). The grid is condensed towards the wall and towards the kink of the

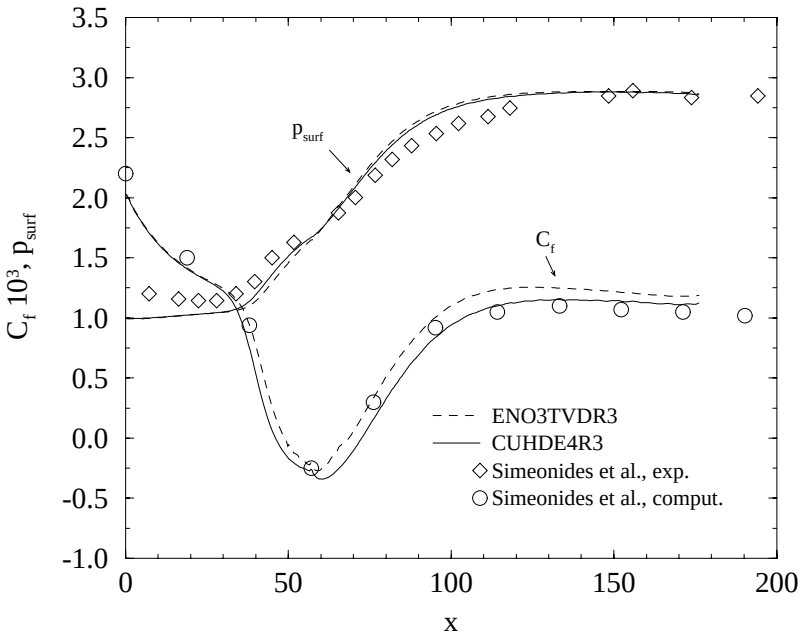

FIGURE 1. Skin friction and surface pressure, 7.5^o laminar compression corner at $M_\infty = 6$. Symbols: ---- , ENO3TVDR3; ——— , CUHDE4R3; $\diamond$, Simeonides *et al.*, exp.; $\circ$, Simeonides *et al.*, comput.

ramp. As initial condition we take outside of the boundary layer the solution of the inviscid deflection problem, while near the wall a boundary layer from a similarity solution is given (ignoring the adverse pressure gradient on the inclined segment of the ramp). As boundary conditions we fix at the inflow the initial condition for all primitive variables giving the correct number of 5 conditions for the Navier-Stokes equations (Oliger & Sundström, 1978). At the outflow we prescribe perfectly non-reflecting boundary conditions (Thompson, 1987). At the upper boundary freestream conditions for all flow variables are prescribed.

The computation is started with $N_x = 151$ and $N_z = 61$. After 1000 iterations with a 3rd order LLF-ENO scheme, the resolution is increased to $N_x = 351$ and $N_z = 121$ and the computation is continued for 12000 time steps. Finally, we switch to the hybrid scheme (5th compact upwind, 4th order LLF-ENO) and continue for another 16000 iterations. For the shock detection parameters we use $\beta_x = 5$ and $\beta_z = 5$. The agreement between the computational and experimental results of Simeonides *et al.* (1994) and the present results is satisfactory, Fig. 1. A small inflow transient is caused by the fact that we prescribe a boundary layer profile at inflow. This is to match the procedure in later DNS. In Simeonides *et al.* (1994) the plate leading edge is included in the computational domain.

Figure 3 shows a quasi-Schlieren plot (merely the norm of the density gradient) when the computations were halted. Both the separation shock and the main ramp shock are clearly visible.

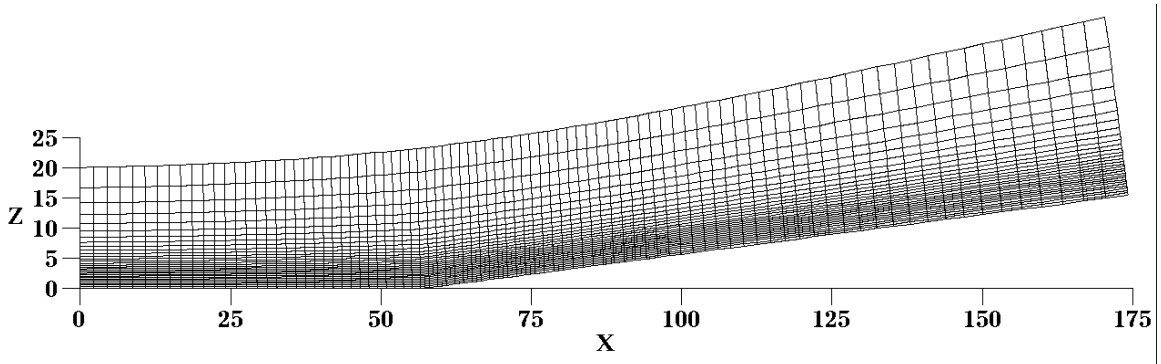

FIGURE 2. Grid for 7.5^o ramp, each 4th grid line shown.

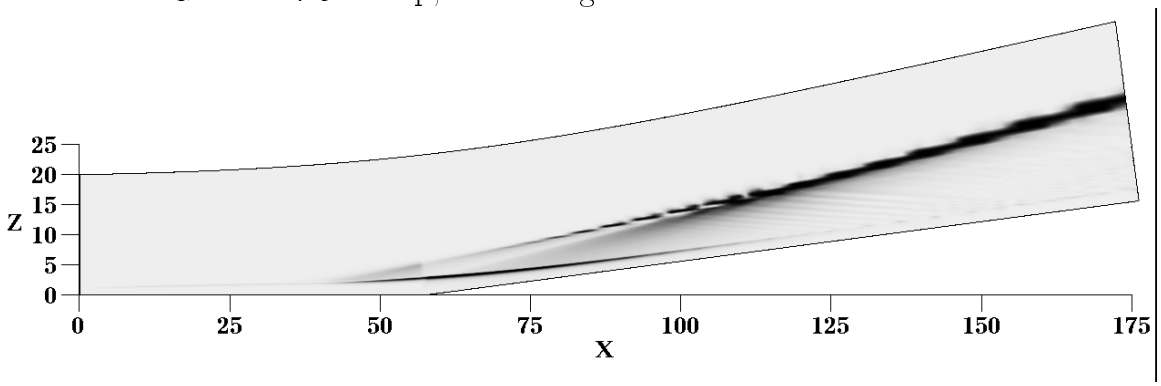

FIGURE 3. Quasi-Schlieren plot (intensity proportional to norm of density gradient).

2.5 Test computation – flat plate

A test computation of a turbulent boundary layer along a flat plate at $M_\infty = 3$ has been performed. The Reynolds number is $Re_{\delta_1} = 10000$, where δ_1 is the laminar displacement thickness corresponding to the inflow station, which is also the reference length. We take as reference length the displacement thickness from a laminar similarity solution since it is uniquely defined corresponding to a downstream station measured from the plate leading edge. The flow parameters are given in Table 2. Discretization is $N_x = 351$, $N_y = 41$ and $N_z = 121$.

The inflow data are generated from the temporal simulation data of Guo and Adams (1994) using Taylor's hypothesis. Initial condition is a laminar similarity solution which is also the reference solution used in the sponge region $48 < x \leq 56$ (Adams, 1994). The computation extends over 8000 time steps. Time step size is about $\Delta_t = 0.1069\ t^+$. The output data are sampled over the final 4400 time steps, starting after the inflow plane has been convected through the outflow. The time sampling interval is about 470 t^+.

For a comparison we refer to the inflow boundary layer profile of the experimental data at higher Reynolds number for a 25^o compression corner of Zheltovodov *et al.* (1990). In Table 3 we compare data from simulation and experiment. In Fig. 4 we compare mean flow profiles (spanwise and ensemble averaged) at the

TABLE 2. Flow parameters for $M_\infty = 3$ flat plate.

quantity	value	comment
T^*_∞	115K	
M_∞	3	
Pr	0.72	
κ	1.4	
R	287.03	
μ^*_∞	$7.98 \cdot 10^{-6}$kg/m/s	
S^*	110.4K	
Re_{δ_1}	10000	
δ^*_1	$4.0830 \cdot 10^{-4}$m	
ξ_0	338.32	inflow station
L_x	56	streamwise box-length
L_y	4	spanwise box-length
L_z	25	wall-normal box-length

TABLE 3. Boundary layer data for flat plate, C_f is the skin friction coefficient, v^+ is the friction velocity, l^+ is the wall unit, Δ^+ is the grid spacing in wall units (for the wall-normal direction z it is the distance of the first point away from the wall), and δ_1 is the turbulent displacement thickness.

quantity	$x = 10.08$	$x = 25.12$	$x = 40.00$	exp
C_f	$0.27 \cdot 10^{-2}$	$0.28 \cdot 10^{-2}$	$0.26 \cdot 10^{-2}$	$0.15 \cdot 10^{-2}$
v^+	0.0595	0.0605	0.0576	0.0442
l^+	0.0107	0.0101	0.0098	0.0075
Δ^+_x	17.41 l^+	18.47 l^+	19.02 l^+	–
Δ^+_y	9.33 l^+	9.89 l^+	10.19 l^+	–
Δ^+_z	4.89 l^+	5.18 l^+	5.34 l^+	–
δ_1	1.53	1.56	1.55	1.93

same streamwise stations as in Table 3 with the experiment.

In general the quality of the simulation data is unsatisfactory. This is due to several reasons. One is the large distance of the first grid point away from the wall, which results in a poor approximation of wall-normal gradients. Another is the relatively small streamwise extent of the computational domain, which is only about 10 turbulent boundary layer thicknesses, considering the fact that the outflow sponge affects about another 1.5 boundary layer thicknesses, even less. The downstream extent of the inflow transient cannot be clearly assessed. Also, we make the same observation as in Guo and Adams (1994) that there is a mass defect visible in the profiles from the simulation in the lower boundary layer half. This

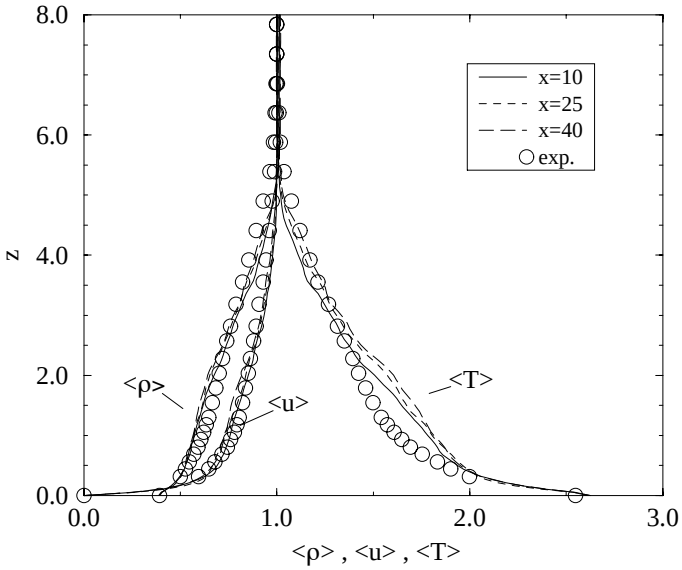

FIGURE 4. Mean flow profiles for $M_\infty = 3$ flat plate. Symbols: ——— , $x = 10$; - - - - , $x = 25$; — — — , $x = 40$; ○ , exp.

is attributed to the too small streamwise extent, which apparently does not allow for the appropriate evolution of streamwise streaks. The computational cost was $32\mu s/(N_{point}\ N_{timestep})$ for a single CRAY C90 CPU.

3. Future plans

From the numerical experiments mentioned in the previous section, we estimate a set of parameters where a direct numerical simulation of a compression corner is feasible. A direct numerical simulation at these parameters will be attempted while an accompanying large-eddy simulation is under consideration by K. Mahesh (CTR).

3.1 DNS parameters and cost estimate

The Reynolds number with respect to the turbulent displacement thickness at inflow is about 6000. Turbulent boundary layer thickness and turbulent displacement thickness can be estimated as about 600 l^+ and 210 l^+, respectively. With an expected discretization of $N_x = 601$, $N_y = 51$, and $N_z = 141$, we estimate $\Delta_x = 15\ l^+$ and $\Delta_z = 10\ l^+$. With an estimated $T_{pass} = 300\ t^+$ for the inflow plane to be convected through the domain, a time step of about $\Delta_t = 0.06\ t^+$, and a code performance of about $38\mu s/(N_{point}\ N_{timestep})$ on a single CRAY C90 CPU, we require an estimated 265 hours per T_{pass}.

Acknowledgments

I acknowledge helpful discussions with K. Shariff, who also helped by reviewing a draft of this report, and R. Moser. For graphics postprocessing the DLR graphics package COMADI has been used.

TABLE 4. Flow parameters for $M_\infty = 3$ ramp.

quantity	value	comment
T^*_∞	115K	
M_∞	3	
Pr	0.72	
κ	1.4	
R	287.03	
μ^*_∞	$7.98 \cdot 10^{-6}$kg/m/s	
S^*	110.4K	
Re_{δ_1}	4000	
δ^*_1	$1.6331 \cdot 10^{-4}$m	reference length
ξ_0	135.33	inflow station
L_1	45	length of first ramp segment
L_2	45	length of second ramp segment
ϕ	18	ramp deflection angle

REFERENCES

Adams, N. A. 1994 Numerical study of boundary layer interaction with shocks – method and code validation. In *CTR Annual Research Briefs 1994*, Center for Turbulence Research, NASA Ames/Stanford Univ.

Adams, N. A. & Shariff, K. 1995 A high-resolution hybrid compact-ENO scheme for shock-turbulence interaction problems. *CTR Manuscript 155*, Center for Turbulence Research, NASA Ames/Stanford Univ. (submitted to *J. Comp. Phys*).

Blaisdell, G. A. & Mansour, N. N. & Reynolds W. C. 1991 Numerical simulations of compressible homogeneous turbulence.*Report* TF-50, Mechanical Engineering, Stanford University, Stanford, California.

Guo, Y. & Adams, N. A. 1994 Numerical investigation of supersonic turbulent boundary layers with high wall temperature. *Proc. 1992 Summer Program*, Center for Turbulence Research, NASA Ames/Stanford Univ.

Oliger, J. & Sundström, A. 1978 Theoretical and practical aspects of some initial boundary value problems in fluid dynamics. *SIAM J. Appl. Math.* **35**, 419–446.

Thompson, K. W. 1987 Time dependent boundary conditions for hyperbolic systems. *J. Comput. Phys.* **68**, 1–24.

Zheltovodov, A. A., Zaylichny, E. G., Trofimov, V. M. & Yakovlev, V. N. 1990 An experimental documentation of supersonic turbulent flows in the vicinity of sloping forward and backward facing steps. In Settles, G. S., & Dodson, L. J. 1994 Supersonic and hypersonic shock / boundary-layer interaction database. *AIAA Journal* **32**, 1377–1383.

ZURMÜHL, R. AND FALK, S. 1984 Matrizen und ihre Anwendungen 1: Grundlagen. Fifth edition, Springer Verlag, Berlin.

Appendix A. Split form of the convective fluxes

A typical indication of underresolution (thus of aliasing errors) of a direct numerical simulation of a compressible flow, solving the compressible Navier-Stokes equations, is the appearance of regions with negative temperature (or pressure). This is related to a local imbalance of internal (potential) and kinetic energy, caused mostly by aliasing errors. It has been observed by Blaisdell *et al.* (1991) that for the pseudospectral computation of derivatives of convolutions of dependent variables, as $\partial(fg)$, the aliasing error is reduced by using the identity $\partial(fg) = 1/2(\partial(fg) + 1/2 + f\partial g + 1/2g\partial f$. For finite-difference schemes the coefficients of the discrete Fourier series for the derivative have to be multiplied by the integer modified wavenumber, which becomes a function of the integer wavenumber; for dissipative schemes this modified wavenumber is complex. In this appendix we briefly investigate the effect of a split form of the convective fluxes for a dissipative finite-difference schemes. From numerical experimentation with coarsely resolved computations for a flat plate, we see that for the upwind scheme used above aliasing errors are even more critical for the split formulation than for the conservative form.

First we derive the expressions for pseudospectral convolution in terms of discrete Fourier series for a Fourier scheme (in the following the summations $\sum_{n+m=k}$ and $\sum_{n+m=k\pm N}$ are always to be taken over $m, n = -N/2, ..., -N/2 - 1$)

$$\partial_x(fg) = \sum_{k=-\frac{N}{2}}^{\frac{N}{2}-1} \mathrm{i}k \left(\sum_{m+n=k} \hat{f}_m \hat{g}_n + \sum_{m+n=k\pm N} \hat{f}_m \hat{g}_n \right) e^{\mathrm{i}kx} \qquad (A.1)$$

and

$$\frac{1}{2}\partial_x(fg) + \frac{1}{2}g\partial_x f + \frac{1}{2}f\partial_x g =$$

$$= \sum_{k=-\frac{N}{2}}^{\frac{N}{2}-1} \left(\sum_{m+n=k} \mathrm{i}\frac{1}{2}(k+m+n)\hat{f}_m \hat{g}_n + \sum_{m+n=k\pm N} \mathrm{i}\frac{1}{2}(k+m+n)\hat{f}_m \hat{g}_n \right) e^{\mathrm{i}kx}$$

$$= \sum_{k=-\frac{N}{2}}^{\frac{N}{2}-1} \left(\sum_{m+n=k} \mathrm{i}k\hat{f}_m \hat{g}_n + \sum_{m+n=k\pm N} \mathrm{i}(k \pm \frac{N}{2})\hat{f}_m \hat{g}_n \right) e^{\mathrm{i}kx} \ . \qquad (A.2)$$

For a finite difference schemes this reads

$$\partial_x(fg) = \sum_{k=-\frac{N}{2}}^{\frac{N}{2}-1} \mathrm{i}\tilde{k}(k) \left(\sum_{m+n=k} \hat{f}_m \hat{g}_n + \sum_{m+n=k\pm N} \hat{f}_m \hat{g}_n \right) e^{\mathrm{i}kx} \qquad (A.3)$$

and

$$\frac{1}{2}\partial_x(fg) + \frac{1}{2}\partial_x fg + \frac{1}{2}f\partial_x g =$$

$$= \sum_{k=-\frac{N}{2}}^{\frac{N}{2}-1} \left(\sum_{m+n=k} \mathrm{i}\frac{1}{2}(\tilde{k}(k) + \tilde{m}(m) + \tilde{n}(n))\hat{f}_m \hat{g}_n + \right.$$

$$\left. + \sum_{m+n=k\pm N} \mathrm{i}\frac{1}{2}(\tilde{k}(k) + \tilde{m}(m) + \tilde{n}(n))\hat{f}_m \hat{g}_n \right) e^{\mathrm{i}kx} \ . \qquad (A.4)$$

Using the symmetry properties of the dispersion function and of the dissipation function, we restrict the following to $0 \leq \xi \leq \pi$. We approximate the modified wavenumber $\tilde{\xi}(\xi)$ piecewise linearly by

$$\tilde{\xi}(\xi) \simeq \begin{cases} \xi & , \text{ if } \xi \leq \Xi \\ \frac{\pi-\xi}{\pi-\Xi}\Xi + \mathrm{i}\frac{\Xi-\xi}{\pi-\Xi}\tilde{D} & , \text{ if } \Xi < \xi \leq \pi \end{cases} \ . \qquad (A.5)$$

The integer modified wavenumber $\tilde{k}(k)$ is then obtained as

$$\tilde{k}(k) \simeq \begin{cases} k & , \text{ if } k \leq K \\ \frac{N-2k}{N-2K}K + \mathrm{i}\frac{2K-2k}{N-2K}D & , \text{ if } K < k \leq \frac{N}{2} \end{cases} \ . \qquad (A.6)$$

For the split formulation we get:
Case (1) $-K \leq k \leq K$:

$$\frac{1}{2}\partial_x(fg) + \frac{1}{2}\partial_x f g + \frac{1}{2} f \partial_x g =$$

$$= \sum_{k=-\frac{N}{2}}^{\frac{N}{2}-1} \left[\mathrm{i} \left(\sum_{m+n=k} \underbrace{k}_{\mathrm{I}} \hat{f}_m \hat{g}_n + \sum_{m+n=k\pm N} \left(k \pm \frac{N}{2} \right) \hat{f}_m \hat{g}_n \right) \right] e^{\mathrm{i}kx} \qquad (A.7)$$

Case (2) $K < k \leq \frac{N}{2}$:

$$\frac{1}{2}\partial_x(fg) + \frac{1}{2} g \partial_x f + \frac{1}{2} f \partial_x g =$$

$$= \sum_{k=-\frac{N}{2}}^{\frac{N}{2}-1} \left[\sum_{m+n=k} \underbrace{-\frac{3K-2k}{N-2K}D}_{\mathrm{VI}} \hat{f}_m \hat{g}_n + \sum_{m+n=k\pm N} \underbrace{-\frac{3K \mp N - 2k}{N-2K}D}_{\mathrm{VII}} \hat{f}_m \hat{g}_n + \right.$$

$$\left. + \mathrm{i} \left(\sum_{m+n=k} \underbrace{\frac{\frac{3}{2}N-2k}{N-2K}K}_{\mathrm{II}} \hat{f}_m \hat{g}_n + \sum_{m+n=k\pm N} \underbrace{\frac{(\frac{3}{2}\mp 1)N-2k}{N-2K}K}_{\mathrm{III}} \hat{f}_m \hat{g}_n \right) \right] e^{\mathrm{i}kx} \ . \qquad (A.8)$$

For the non-split formulation we get:
Case (1) $-K \leq k \leq K$:

$$\partial_x(fg) =$$

$$= \sum_{k=-\frac{N}{2}}^{\frac{N}{2}-1} \left[\mathrm{i} \left(\sum_{m+n=k} \underbrace{k}_{\mathrm{IV}} \hat{f}_m \hat{g}_n + \sum_{m+n=k\pm N} k \hat{f}_m \hat{g}_n \right) \right] e^{\mathrm{i}kx} \qquad (A.9)$$

Case (2.) $K < k \leq \frac{N}{2}$:

$$\partial_x (fg) =$$

$$= \sum_{k=-\frac{N}{2}}^{\frac{N}{2}-1} \left[\sum_{m+n=k} \underbrace{-\frac{2K-2k}{N-2K} D}_{\mathrm{VIII}} \hat{f}_m \hat{g}_n + \sum_{m+n=k\pm N} -\frac{2K-2k}{N-2K} D \hat{f}_m \hat{g}_n + \right.$$

$$\left. + \mathrm{i} \left(\sum_{m+n=k} \underbrace{\frac{N-2k}{N-2K} K}_{\mathrm{V}} \hat{f}_m \hat{g}_n + \sum_{m+n=k\pm N} \frac{N-2k}{N-2K} K \hat{f}_m \hat{g}_n \right) \right] e^{\mathrm{i}kx} \ . \qquad (A.10)$$

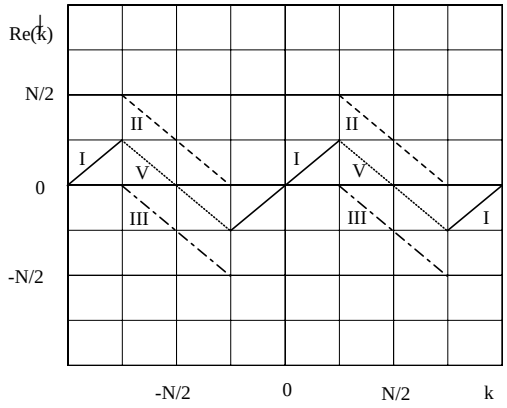

FIGURE 5. Sketch of the dispersion for non-split and split formulation.

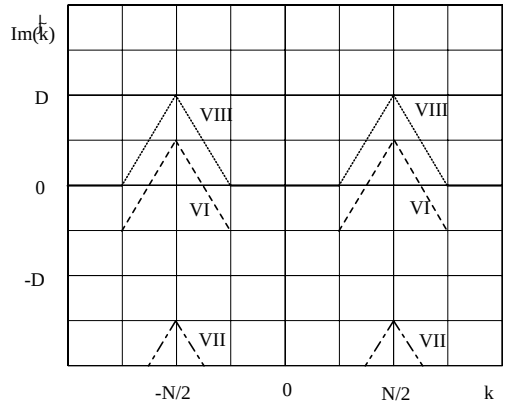

FIGURE 6. Sketch of the dissipation for non-split and split formulation.

The factors in the above Fourier sums have character of modified wavenumbers and represent the wave properties (dispersion and dissipation) of the particular Fourier mode. We now inspect particular factors. Considering the first terms on the left-hand sides first, we see that the split formulation generates the spurious wave (II,VI) while the non-split formulation generates (V,VIII). From the dispersion shown in Fig. 5 it is evident that II and V contribute by aliasing to the resolved spectrum. The spurious waves (II,VI) from the split formulation however, are partially amplified (negative dissipation) while the spurious waves from the non-split formulation are damped. From the second terms on the right-hand side we see that the split formulation generates another pair of spurious waves which contribute to the resolved spectrum by aliasing which is also amplified (III,VII). We conclude that the non-split formulation for an upwind scheme can exhibit spurious waves which are amplified contrary to the non-split form. This is due to the fact that the modified wavenumber for dissipative schemes is complex.